

Multifunctional iron-based Metal – Organic framework as biodegradable nanozyme for microwave enhancing dynamic therapy

Xiaoyan Ma^{a,b}, Xiangling Ren^a, Xudong Guo^b, Changhui Fu^a, Qiong Wu^a, Longfei Tan^{a,*}, Hongbo Li^c, Wei Zhang^d, Xudong Chen^d, Hongshan Zhong^{e,***}, Xianwei Meng^{a,*}

^a Laboratory of Controllable Preparation and Application of Nanomaterials, Laboratory of Cryogenics, Technical Institute of Physics and Chemistry, Chinese Academy of Sciences, 29 Zhongguancun East Road, Beijing, 100190, China

^b State Key Laboratory of Reproductive Regulation & Breeding of Grassland Livestock, Inner Mongolia University, 24 Zhaojun Road, Hohhot, 010070, China

^c Beijing Key Laboratory of Construction-Tailorable Advanced Functional Materials and Green Applications, School of Materials Science & Engineering, Beijing Institute of Technology, Beijing, 100081, China

^d First Affiliated Hospital of Southern University of Science and Technology, Shenzhen People's Hospital & Shenzhen Interventional Medical Engineering Research and Development Center, Shenzhen, 518020, China

^e Department of Radiology, First Hospital of China Medical University, Shenyang, 110001, People's Republic of China

ARTICLE INFO

Keywords:

Nanozyme
Metal-organic framework
Enzyme mimics
Microwave
Cancer therapy

ABSTRACT

Nanozymes with excellent enzyme-mimicking catalytic property are playing an increasingly significant role in tumor diagnosis and therapy. Fe-metal organic framework nanoparticles (MIL-101(Fe) NPs) are prepared as nanozymes to generate reactive oxygen species (ROS) and induce cancer cell death by catalyzing endogenous substances in tumor microenvironment. Abundant stimuli-responsive hydroxyl radicals ($\cdot\text{OH}$) are accelerated to generate in the presence of microwave irradiation, realizing microwave enhancing dynamic therapy (MEDT). Moreover, MIL-101(Fe) NPs possess biodegradability and bioreponsibility, which exhibit favourable properties of metabolism and non-toxic accumulation comparing with inorganic nanozymes. Fluorescent gold nanoclusters (BSA-Au NCs) are rapidly coupled with the surface of MIL-101(Fe) NPs to obtain MIL-101(Fe)@BSA-AuNCs NPs. MIL-101(Fe)@BSA-AuNCs NPs with magnetic resonance imaging (MRI) and fluorescent imaging (FI) not only image accurately for the site of tumor, but also monitor dynamic distribution process of MIL-101(Fe) *in vivo*. The signal intensity of FI and MRI reaches maximum at 1 h in the liver and 5 h in the tumor. Ionic liquid (IL) is also loaded into MIL-101(Fe)@BSA-AuNCs NPs as microwave sensitive reagents for microwave thermal therapy (MTT). This work synthesizes the nanozymes that possess degradability, microwave sensitivity and dual-mode imaging to achieve the combination of MTT and MEDT against tumor. Experiment result *in vivo* confirms that the kill rate of tumor is up to 96.65%, showing an outstanding anti-tumor efficacy.

1. Introduction

Nanozymes, which possess desirable enzyme-mimicking catalytic property based on nanomaterials, have sparked increasing interest from cross-disciplinary scientific community in recent years [1–5], for example, iatrology, environmental protection, and materialogy, etc. In iatrology field, increasing nanozymes have been applied for tumor diagnostic imaging [6–8], enhancing radiotherapy efficiency [9,10]. Moreover, nanozymes have been reported for dynamic therapy, for example, enhancing photodynamic therapy [11,12], and chemodynamic therapy (CDT) [13]. CDT has been achieved by catalyzing

endogenous chemical energy to generate reactive oxygen species without external energy, which induce cell death. Although CDT is promising, research teams still need find new strategies to improve the generation rate of hydroxyl radicals ($\cdot\text{OH}$) in tumor site and effectively control the process of tumor treatment, realizing precise treatment ultimately. To achieve effective, controllable and precise treatment, external stimulation is primary choice. Hence, it is of great importance to find an idea external stimulus for future clinical application.

Microwave (MW), as a clinical tumor treatment method, possesses advantages of low side effect and deep penetration, which is an ideal external stimulus [14,15]. Thus, it is desired to apply external stimulus

* Corresponding author.

** Corresponding author.

*** Corresponding author.

E-mail addresses: longfeitan@mail.ipc.ac.cn (L. Tan), hszhong@cmu.edu.cn (H. Zhong), mengxw@mail.ipc.ac.cn (X. Meng).

of MW to generate $\cdot\text{OH}$ in a more efficient way. Abundant $\cdot\text{OH}$ in the tumor microenvironment are accelerated to generate in the presence of MW irradiation, which is defined as microwave enhancing dynamic therapy (MEDT). Hence, it is crucial to design and synthesize nanozymes with MW response for the generation of $\cdot\text{OH}$ and realizing MEDT.

The metal-organic framework nanoparticles (MOF NPs) with tunable porous structure and high specific surface area have great potential to act as MW sensitive agents, which promote the MW energy conversion owing to ions collision in the porous structure of MOF [14,16]. Meanwhile, it is well known that iron-based compounds possess peroxidase-like catalytic activity [17]. Therefore, it is promising to design and synthesize Fe based MOF NPs with both MW response and catalytic property as nanozymes. What's more, MOF NPs possess good degradability, which have unique application function for drug release as biosafe therapeutic nanoagents [18,19]. Comparing with reported undegradable inorganic nanozymes (MnO_2 , Fe_3O_4), degradable MOF nanozymes decrease significantly the toxicity *in vivo* [20,21]. Furthermore, MOF nanozymes as a nanocarrier system possess bioresponsibility based on the unique physicochemical property to accomplish enhanced therapeutic specificity and simplicity [22–26]. The biocompatible and biodegradable nanozymes promote great progress in biomedical applications of cancer theranostics [27]. MOF NPs are composited initially multi-functional composite nanomaterials to apply for tumor therapy [16,28–52]. Especially, MOF NPs as nanozymes can play high multifunctional efficiency against tumor by combining with the properties of MOF NPs [53–55].

To achieve the aforementioned aims for tumor therapy, we have designed Fe-metal organic frameworks (MIL-101(Fe)) as nanozymes with degradability for tumor therapy (Scheme 1). MIL-101(Fe) mimicking enzymes are capable of catalyzing H_2O_2 in tumor microenvironment to generate $\cdot\text{OH}$. Under MW irradiation, amounts of $\cdot\text{OH}$ are generated into the tumor with an efficient and noninvasive manner, which realizes MEDT. Meanwhile, a rapid assembly method was adopted to achieve the coupling of fluorescence gold nanoclusters (BSA-Au NCs) on surface of IL@MIL-101(Fe) NPs without the presence of fluorescence quench to obtain MIL-101@BSA-AuNCs NPs. Magnetic resonance imaging (MRI) and fluorescence imaging (FI) of MIL-101(Fe)

@BSA-AuNCs NPs are used for monitoring dynamics distribution process of MIL-101(Fe) NPs *in vivo* and accurately diagnosing tumor site. The signal intensity of FI and MRI becomes weak gradually because of significant structural collapse of MIL-101(Fe) NPs. Due to the porous structure, 1-octyl-3-methylimidazolium hexafluorophosphate (IL) are loaded on MIL-101(Fe) NPs to prepare IL@MIL-101(Fe)@BSA-AuNCs NPs as thermal sensitization agents, achieving tumor synergetic therapy of microwave thermal therapy (MTT) and MEDT. IL@MIL-101(Fe)@BSA-AuNCs NPs mainly set synergetic therapy and imaging together, which have inestimable value for future clinical application.

2. Experimental section

2.1. Synthesis of MIL-101(Fe) NPs

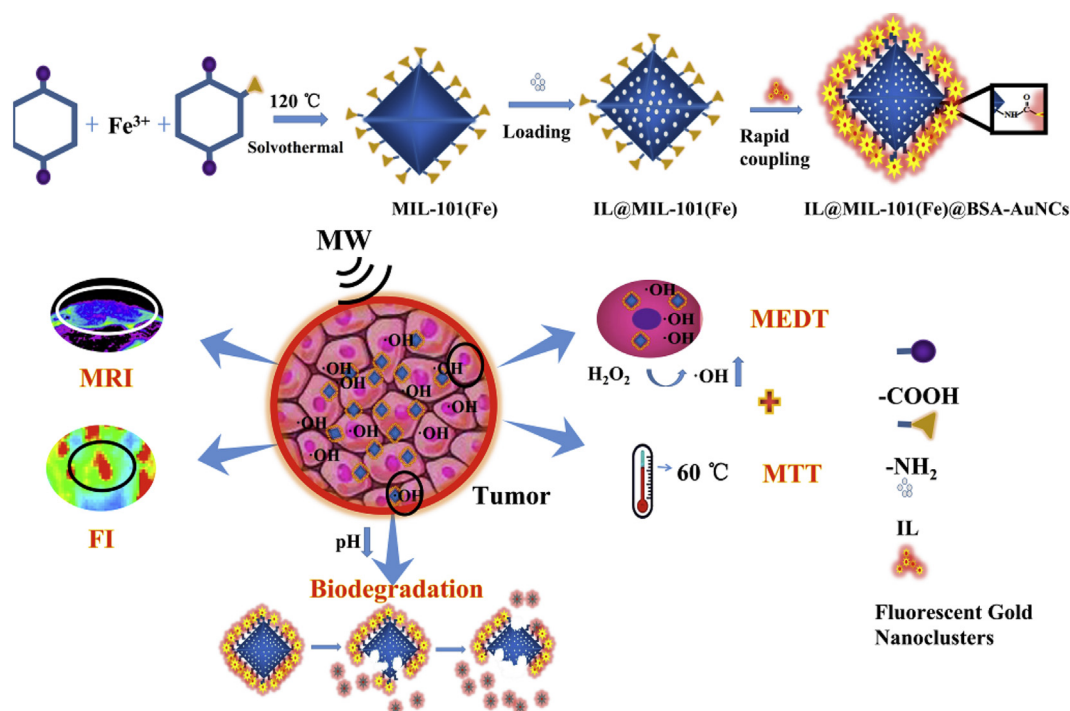
The MIL-101(Fe) NPs were prepared by solvothermal method. 0.0601 g of H_2BDC , 0.0611 g of $\text{H}_2\text{BDC-NH}_2$, and 0.0676 g of $\text{FeCl}_3 \cdot 6\text{H}_2\text{O}$ were dissolved in 100 mL of DMF, the mixed solution was packaged in teflon-lined stainless-steel autoclave and heated to 120 °C for 12 h in an oven. The precipitate obtained by centrifugation was washed three times with ethanol after cooling to room temperature.

2.2. Synthesis of IL@MIL-101(Fe) NPs

10 mg of MIL-101(Fe) NPs were dispersed in 3 mL of diethylene dioxide solution, then 100 μL of IL were added. The mixture was stirred for 2 h in the dark. IL@MIL-101(Fe) NPs were collected and washed with ethanol twice by centrifugation.

2.3. Synthesis of BSA-Au NCs

300 mg of bovine serum albumin (BSA) were dissolved in 6 mL of H_2O , and 8 mL of 10 mM chloroauric acid was added to the mixture. After stirring for 2 min, 0.65 mL of 1 M NaOH was added. The mixture was placed in oven at 100 °C and allowed to stand for 1 h after stirring.



Scheme 1. Experiment schematic. Schematic shows the synthesis of IL@MIL-101(Fe)@BSA-AuNCs NPs, degradation process of IL@MIL-101(Fe)@BSA-AuNCs NPs, therapy process of IL@MIL-101(Fe)@BSA-AuNCs NPs *in vivo*.

2.4. Synthesis of IL@MIL-101(Fe)@BSA-AuNCs NPs

2 mL of fluorescent gold nanoclusters were dispersed in 15 mL of H₂O and activated by stirring with 1 mL of EDC and NHS for 15 min. When the temperature reached 60 °C, 5 mg of IL@MIL-101(Fe) NPs were added with stirring for 60 s. IL@MIL-101(Fe)@BSA-AuNCs NPs were separated by centrifugation and washing with H₂O.

2.5. IL@MIL-101(Fe) NPs MW heating experiment in vitro

Microwave heating experiment confirmed that the IL@MIL-101(Fe) NPs possessed MW thermal sensitizing property. The IL@MIL-101(Fe) NPs were formulated with saline into different concentrations of 1, 3, 5, 7, and 10 mg mL⁻¹, and then normal saline was used as control group, and 1.0 mL each was added to the reaction hole and irradiated at 0.9 W for 5 min. The forward-looking infrared (FLIR) imaging instrument was used to monitor the temperature change while accompanied by infrared imaging. Meanwhile the thermal sensitivity of IL@MIL-101(Fe) NPs with gold clusters coupled with the outer layer (IL@MIL-101(Fe)@BSA-AuNCs NPs) were not changed.

2.6. Microwave enhancing dynamics experiment of MIL-101(Fe) NPs in vitro

In this experiment, the MIL-101(Fe) NPs were dispersed in H₂O to avoid the heating effect, exhibiting no increase in temperature under MW irradiation. For the detection of ·OH, TMB detection solution was prepared by using 1 mL of DMSO liquid to disperse 10 mg of TMB. 20 µL of TMB, 25 µg mL⁻¹ of MIL-101(Fe) NPs and 5 µL of H₂O₂ were dispersed in water and then supernatants were analyzed by UV-vis spectroscopy every 5 min. Under the same condition, the mixed solution in reaction vessel was irradiated with 0.9 W MW for 5 min. The mixed solution was then analyzed every 5 min by UV-vis spectroscopy. In the same manner, the ultraviolet absorption of 2, 4, 6, and 8 µL of different volumes of H₂O₂ before and after MW was measured. Finally, in the same condition, the ultraviolet absorption of 0.02, 0.04, 0.06, and 0.08 µg mL⁻¹ of MIL-101(Fe) NPs before and after MW irradiation was measured.

10 mg of terephthalic acid (TA) were dispersed in DMSO to prepare TA solution. 50 µg mL⁻¹ of MIL-101(Fe) NPs were dispersed in water with 20 µL TA solution and 10 µL of H₂O₂, and then the intensity of fluorescence was tested. In the same situation, the intensity of fluorescence was tested under MW irradiation at 0.9 W for 5 min. The intensity of fluorescence under MW irradiation and no MW irradiation was compared, and the intensity of fluorescence was recorded under MW irradiation for 3, 5, 10, 15 min by fluorescence spectrophotometry.

ESR was applied to test the generation of ·OH by 5, 5'-dimethylpyrroline-N-oxide. 5 µL of H₂O₂ was dispersed in H₂O with MW irradiation, and 5 µL of H₂O₂ and 50 µg of MIL-101(Fe) NPs were dispersed in H₂O with MW irradiation. ESR spectrums from two groups were collected.

2.7. Experimental study on degradation of MIL-101(Fe) NPs in vitro

It has been confirmed that the tumor site is acidic by consulting other research literature. Therefore, the degradation experiment of MIL-101(Fe) NPs was taken carry out in acidic PBS solution. The appropriate amount of MIL-101(Fe) NPs were dispersed in acidic PBS solution and placed in a constant temperature water bath at 37 °C. The sample was taken different time points for TEM characterization and size measurement. Degradation experiment proved that the MIL-101(Fe) NPs were degradable.

2.8. Cytotoxicity experiment in vitro

In order to investigate the toxicity of the as-made IL@MIL-101(Fe)

@BSA-AuNCs NPs, the MTT assay was used to explore on HepG2, L929, H22 cells. The cytotoxicity of IL@MIL-101(Fe)@BSA-AuNCs NPs was judged by the cell viability after incubated with different concentrations of IL@MIL-101(Fe)@BSA-AuNCs NPs. Firstly, the cells were uniformly dispersed in 96-well plate. After the cells were adherent, then cells were incubated with different concentrations (1.5625, 3.125, 6.25, 12.5, 50, 100, 200 µg mL⁻¹) for 24 h. Cell viability was evaluated as the absorbance of formazan at 492 nm. The control group cells (without nanomaterials) were considered to be 100 % of survival rate.

2.9. Cell experiments in vitro

To access the efficacy by combination of MEDT and MTT, cell experiment was explored. Tumor cells were incubated with 100 µg mL⁻¹ of IL@MIL-101(Fe)@BSA-AuNCs NPs for 24 h. The cells were irradiated with 0.9 W for 3, 5 and 8 min, then the cell relative activity was accessed by MTT assay. MW group and IL@MIL-101(Fe)@BSA-AuNCs + MW group verified the anti-tumor effect of IL@MIL-101(Fe)@BSA-AuNCs by combining MEDT with MTT.

2.10. Animal toxicity experiment

To further evaluate to the maximum safe dose of IL@MIL-101(Fe)@BSA-AuNCs NPs in mice, animal toxicity experiment was studied. After the preliminary experiment, 20 experimental mice were selected and divided into 4 groups. IL@MIL-101(Fe)@BSA-AuNCs NPs were injected into the mice at doses of 100, 150 and 200 mg kg⁻¹, mice injected PBS were used as control. After 15 days, mouse blood was collected for further routine blood and blood chemistry examinations. At the same time, the heart, spleen, liver, lungs and kidneys were soaked in formalin solution for further histological examination. Tissue sections of mouse organs with different doses of material were contrasted to observe the difference.

2.11. Tumor therapy experiment

The anti-cancer effect of IL@MIL-101(Fe)@BSA-AuNCs NPs by combining with MDT and MTT at mice was further evaluated. When the tumor diameter of female mice bearing H22-tumor was about 8 mm, experimental mice were randomly divided into the following four groups: (1) control group, (2) MW, (3) IL@MIL-101(Fe)@BSA-AuNCs, (4) IL@MIL-101(Fe)@BSA-AuNCs + MW (The control group was injected with PBS). The injection dose was 50 mg kg⁻¹ and the above materials were injected into the mice through the tail vein. After 5 h of injection, MW irradiation was performed for microwave experimental groups with 0.9 W for 5 min, and the process of temperature change was recorded by FLIR imaging instrument. The mice were recorded daily for body weight and tumor volume. At the end of the experiment, heart, spleen, liver, lungs, and kidneys of mice were soaked in formalin solution for further histological examination to observe the histological section of the mouse organs.

2.12. Animal experiments

All animal studies were approved by Guide for the Care and Use of Laboratory Animals, Eighth Edition (International Publication No: 978-0-309-15400-0) and was approved by the Institutional Animal Care and Use Committee (IACUC) of the Chinese PLA General Hospital Animal Care and Use Committee.

3. Results and discussion

3.1. Synthesis and characterization of IL@MIL-101(Fe)@BSA-AuNCs

IL@MIL-101(Fe)@BSA-AuNCs NPs were synthesized through three steps: first, MIL-101(Fe) NPs were prepared by the solvothermal

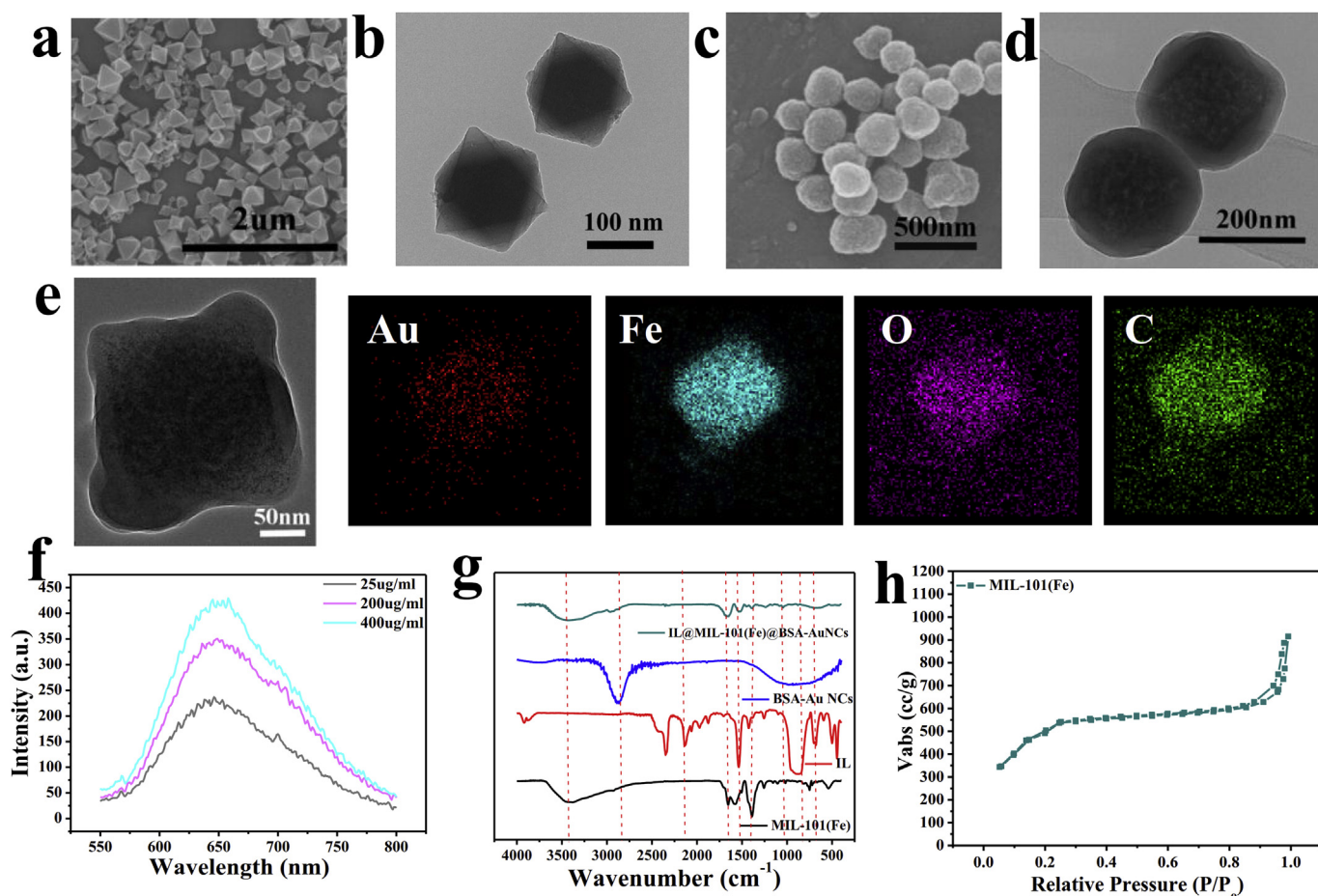


Fig. 1. The characterization of MIL-101(Fe), IL@MIL-101(Fe)@BSA-AuNCs NPs. (a) SEM, (b) TEM images of MIL-101(Fe) NPs. (c) SEM, (d) TEM image of IL@MIL-101(Fe)@BSA-AuNCs NPs. (e) HRTEM-mapping images and the elemental mapping of Au, Fe, O, and C of IL@MIL-101(Fe)@BSA-AuNCs. (f) Fluorescence spectra of 25, 200, 400 $\mu\text{g mL}^{-1}$ IL@MIL-101(Fe)@BSA-AuNCs NPs. (g) FT-IR spectra of IL, BSA-Au NCs, MIL-101(Fe) and IL@MIL-101(Fe)@BSA-AuNCs NPs. (h) N_2 isothermal adsorption-desorption curves of MIL-101(Fe) NPs.

method [54–56]. MIL-101(Fe) NPs possessed good dispersibility, uniform size. The size of MIL-101(Fe) NPs measured by scanning electron microscope (SEM) (Fig. 1a) and transmission electron microscopy (TEM) was around 150 nm (Fig. 1b). The dynamic light scattering was used to measure the average hydrodynamic diameter of MIL-101(Fe) NPs, showing 170.6 nm (Fig. S1a). In the second step, IL with excellent MW heating effect was loaded into MIL-101(Fe) NPs to prepare IL@MIL-101(Fe) NPs [59]. As-made IL@MIL-101(Fe) NPs also possessed the property of MW sensitization. The element mapping of F and P in IL@MIL-101(Fe) NPs manifested IL was successfully loaded into MIL-101(Fe) NPs (Fig. S2). Au NPs had more and more application in catalytic reaction, sensitive detection, and diagnostics [59–62]. Thence, BSA-Au NCs were chose basing on the hydrophilicity and security of BSA-Au NCs. In the third step, BSA-Au NCs were prepared according to the initial literature, which showed excitation and emission peaks at 544 nm and 640 nm [63]. BSA-Au NCs were coupled with the surface of the as-made IL@MIL-101(Fe) NPs by coupling method to synthesize IL@MIL-101(Fe)@BSA-AuNCs NPs, which possessed the fluorescence property. The shape of IL@MIL-101(Fe)@BSA-AuNCs NPs was approximate sphere, which could be observed from SEM (Fig. 1c) and TEM (Fig. 1d). The hydrodynamic diameter of IL@MIL-101(Fe)@BSA-AuNCs was 261.9 nm by dynamic light scattering (Fig. S1b). To further investigate whether the BSA-Au NCs were coupled with the surface of IL@MIL-101(Fe), the element mapping were carried out. The element mapping of Au, Fe, O, and C in IL@MIL-101(Fe)@BSA-AuNCs was showed in Fig. 1e, it demonstrated the BSA-Au NCs were successfully coupled with the surface of IL@MIL-101(Fe). The fluorescent IL@MIL-

101(Fe)@BSA-AuNCs NPs were similar to BSA-Au NCs with emission peak at 640 nm. The fluorescence spectra of IL@MIL-101(Fe)@BSA-AuNCs NPs were gradually increased with the concentration from 25 to 400 $\mu\text{g mL}^{-1}$. As the concentration increased, the fluorescence intensity also increased (Figs. 1f and S3a). IL@MIL-101(Fe)@BSA-AuNCs NPs possessed good stability in PBS (pH = 7.4) and DMEM (with 5% serum) at 0–10 h and exhibited subsidence at 20 h (Fig. S4). Fourier Transform Infrared Spectroscopy was used to analyze the functional groups of IL, BSA-Au NCs, MIL-101(Fe) and IL@MIL-101(Fe)@BSA-AuNCs. The mainly characteristic peak of IL was 1567 cm^{-1} , showing the vibration of the imidazole skeleton. The normal characteristic peak of IL at 674 cm^{-1} was showed. Especially, the characteristic peak of IL appeared at 845 cm^{-1} , which showed the stretching vibration of P–F bond. Above all, it indicated IL was loaded successfully into MIL-101(Fe) NPs. Mainly characteristic peak of BSA-Au NCs was 2877 cm^{-1} , which exhibited in IL@MIL-101(Fe)@BSA-AuNCs. The characteristic peaks of MIL-101(Fe) NPs were 3402 cm^{-1} and 1396 cm^{-1} , which represented amino group and vibration absorption of benzene ring. The main characteristic peaks of IL, BSA-AuNCs and MIL-101(Fe) were exhibited in IL@MIL-101(Fe)@BSA-AuNCs (Fig. 1g). As Fig. 1h shown that the specific surface area of MIL-101(Fe) NPs was $1861.5\text{ m}^2/\text{g}$ and the specific surface area of IL@MIL-101(Fe) NPs was $827.2\text{ m}^2/\text{g}$ (Fig. S3b). The total weight losses of MIL-101(Fe) and IL@MIL-101(Fe) were 36.94% and 31.27%, thus the loading amount of IL was 5.67% by calculating the TGA curves of MIL-101(Fe) and IL@MIL-101(Fe) (Fig. S3c). BET and TGA results indicated that IL were loaded successfully into MIL-101(Fe) NPs. The pattern of MIL-101(Fe), IL@

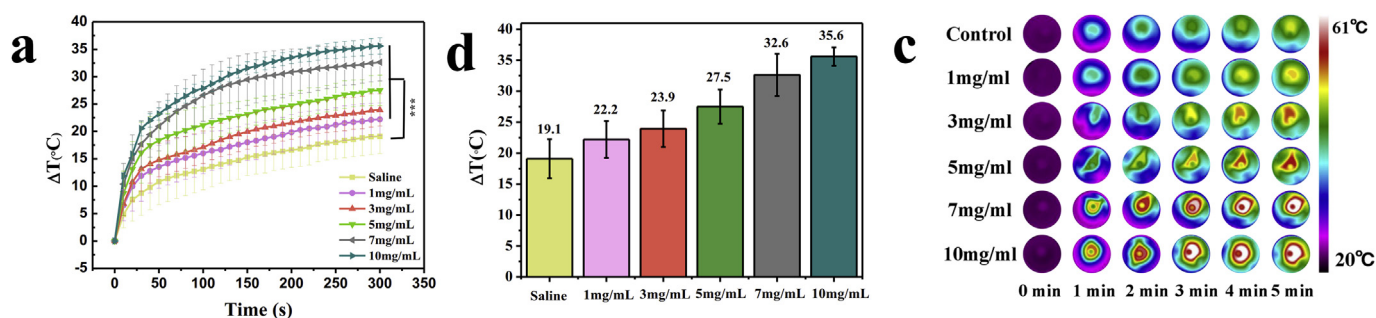


Fig. 2. Microwave thermal therapy experiment of IL@MIL-101(Fe) *in vitro*. (a) Heating curves of the different concentrations of IL@Fe-MOF NPs and IL@MIL-101(Fe) NPs under MW irradiation at a power of 0.9 W for 5 min. (b) Temperature change value based on (a). (c) FLIR images of change process of corresponding temperature. (***) indicates $p < 0.001$.

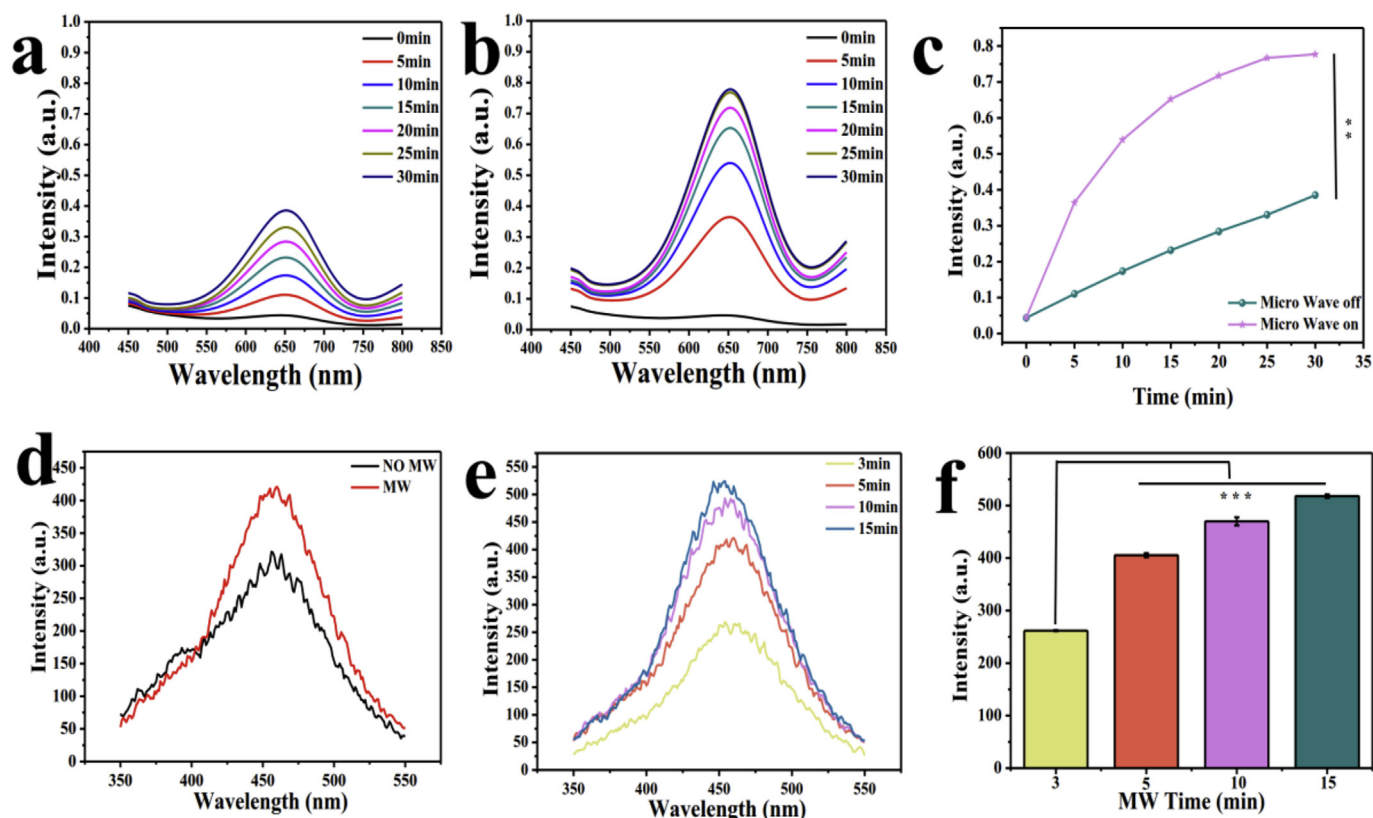


Fig. 3. The evaluation of microwave enhancing dynamic effect. (a), (b) UV-Vis absorb spectra of different time points about MIL-101(Fe) + H₂O₂ + TMB dispersed in water without MW and with MW after irradiation. (c) The histogram of intensity-time dependence of the maximum absorption at 650 nm. (d) The fluorescence spectroscopy of 2-hydroxyterephthalic acid under MW irradiation at 0.9 W for 5 min comparing with no MW irradiation. (e) The fluorescence spectroscopy of 2-hydroxyterephthalic acid under MW irradiation for different time. (f) The intensity of fluorescence under MW irradiation for different time. (** indicates $p < 0.01$, *** indicates $p < 0.001$).

MIL-101(Fe) and IL@MIL-101(Fe)@BSA-AuNCs detected by X-ray diffractometry showed powder pattern of MIL-101(Fe) at low angles of 5.3°, 9.2° and IL@MIL-101(Fe) at low angles of 10.5°, IL@MIL-101(Fe)@BSA-AuNCs with weak diffraction broad peaks. It indicated MIL-101(Fe) NPs were synthesized and IL@MIL-101(Fe)@BSA-AuNCs NPs have their low crystallinity (Fig. S5) [56,58,65,66]. Above all, IL@MIL-101(Fe)@BSA-AuNCs NPs were successfully synthesized.

3.2. IL@MIL-101(Fe) and IL@MIL-101(Fe)@BSA-AuNCs NPs microwave thermal therapy experiment *in vitro*

The hyperthermia in tumor site can effectively destroy tumor cells, IL with excellent MW heating effect is loaded into MIL-101(Fe) NPs. Thus MW sensibility of IL@MIL-101(Fe) NPs need be confirmed under

MW irradiation. It has been confirmed that MW sensitizer dispersed in saline could cause ions high collision frequency under MW irradiation, resulting in the temperature increasing obviously [14,15]. During the experiment, different concentrations of IL@MIL-101(Fe) NPs (1, 3, 5, 7, and 10 mg mL⁻¹) were prepared. 1 mL mixed solution was under 0.9 W MW irradiation for 5 min, 1 mL of saline was used as the control group. From Fig. 2a, the temperature of control group was increased to 19.1 °C after MW irradiation. In the same condition, the temperature of IL@MIL-101(Fe) NPs was increased to 22.2, 23.9, 27.5, 32.6 and 35.6 °C, when the concentration was 1, 3, 5, 7, 10 mg mL⁻¹. Compared with the control group, the temperature was increased by 3.1, 4.8, 8.4, 13.5 and 16.5 °C, the data proved that IL@MIL-101(Fe) NPs possessed MW heating sensibility (Fig. 2b). The FLIR imaging instrument was used to record the change process of corresponding temperature

(Fig. 2c). The MW heating sensibility of IL@MIL-101(Fe)@BSA-AuNCs NPs did not change with BSA-Au NCs coupling with the surface of IL@MIL-101(Fe) NPs (Fig. S6). Therefore, the IL@MIL-101(Fe)@BSA-AuNCs NPs possessed MW sensitivity to increase temperature under MW irradiation and provide energy for generation of ROS, which could be used for MTT *in vivo* [67,68].

3.3. Evaluation of microwave enhancing dynamic therapy effect *in vitro*

Interestingly, it was found that MIL-101(Fe) NPs with peroxidase-like catalytic activity could catalyze H_2O_2 to generate $\cdot\text{OH}$. Meanwhile, abundant $\cdot\text{OH}$ could be accelerated to generate under MW irradiation. The generation of $\cdot\text{OH}$ was tested by 3, 3', 5, 5'-tetramethylbenzidine (TMB) with emerging blue and absorption peak at 652 nm, because TMB could be oxidized by $\cdot\text{OH}$ [14,69]. To avoid accelerative generation of $\cdot\text{OH}$ due to thermal effect under MW irradiation, MIL-101(Fe) NPs were dispersed in water, there was no obvious increase in temperature even under MW irradiation for 5 min (Fig. S7).

When $10\ \mu\text{L}\ \text{H}_2\text{O}_2$ were added in $50\ \mu\text{g mL}^{-1}$ of MIL-101(Fe) NPs and TMB mixing solution and the UV spectrometer was allowed to measure immediately. As the time went on, the intensity of ultraviolet absorption at 652 nm was gradually increased (Fig. 3a). Under the same condition, the intensity of ultraviolet absorption at 652 nm became stronger (Fig. 3b) under MW irradiation at power of 0.9 W for 5 min than that of no MW irradiation. It could be seen obviously that the absorbance after MW irradiation was higher than that without MW irradiation at the same time point (Fig. 3c). Abundant $\cdot\text{OH}$ were accelerated to generate under the MW irradiation, the production rate gradually was slow as time went on. MEDT effect was also demonstrated from different volume of H_2O_2 and amount of MIL-101(Fe) NPs (Fig. S8).

To evaluate the MEDT effect of MIL-101(Fe) NPs overall, TA was also used as $\cdot\text{OH}$ trapping agent to synthesize 2-hydroxyterephthalic acid with excitation wavelength at 315 nm and emission peaks at 450 nm by fluorescence spectrophotometry [70]. As shown in Fig. 3d that the fluorescence intensity was improved under MW irradiation at power of 0.9 W for 5 min comparing with no MW irradiation. The intensity of fluorescence was gradually increasing with the microwave time extending, but fluorescence intensity increased slowly (Fig. 3e and f). The results confirmed that MIL-101(Fe) NPs could catalyze H_2O_2 to generate abundant $\cdot\text{OH}$ with the rapid under MW irradiation, showing the excellent MEDT effect.

ESR was also used to detect more accurately the generation of $\cdot\text{OH}$. The ESR signal was not detected after H_2O_2 dispersing in H_2O with MW irradiation. While the ESR signal was observed after H_2O_2 and MIL-101(Fe) NPs dispersing in H_2O after MW irradiation (Fig. S9).

3.4. Biodegradability experiment of MIL-101(Fe) NPs *in vitro*

The biodegradation and biosafety of MIL-101(Fe) NPs determine clinical application in the future [2]. The degradability of MIL-101(Fe) NPs was verified *in vitro* by incubating MIL-101(Fe) NPs in neutral phosphate buffer (pH = 7.4 PBS) and acid phosphate buffer (pH = 5.5 PBS) [71]. As shown in Fig. 4a, the structure of MIL-101(Fe) was not almost degraded in neutral phosphate buffer, indicating MIL-101(Fe) were stable. While MIL-101(Fe) NPs had the degradable tendency in acid phosphate buffer, and the structure evolution of MIL-101(Fe) NPs was monitored by TEM observations at different time points (1, 5 and 10 h) (Fig. 4b). After incubation for 1 h, the morphology of MIL-101(Fe) NPs remained its original shape. When incubation time reached 5 h, the structure of MIL-101(Fe) NPs started to exhibit degradable tendency. While incubating for 10 h, the structure of MIL-101(Fe) NPs exhibited significant structural collapse, the intact structure of MIL-101(Fe) NPs could hardly be seen. The results manifested that MIL-101(Fe) NPs were degradable, which is promising for the future clinic application.

3.5. Toxicity experiment of IL@MIL-101(Fe)@BSA-AuNCs NPs

The biosafety of nanomaterials was crucial in biomedical application, so the biosafety and compatibility were evaluated at cells and mice respectively. In order to detect the toxic effect of IL@MIL-101(Fe)@BSA-AuNCs NPs, cellular activity of different concentrations (1.5625 , 3.125 , 6.25 , 12.5 , 25 , 50 , 100 , $200\ \mu\text{g mL}^{-1}$) of the IL@MIL-101(Fe)@BSA-AuNCs NPs were evaluated in the HepG2 cells, H22 cells and L929 cells. The toxicity of IL@MIL-101(Fe)@BSA-AuNCs NPs at cells was accessed by methyl thiazolyl tetrazolium (MTT) assay. As shown in Fig. 5a, the relative activity of the cells hardly decreased obviously as the concentration of IL@MIL-101(Fe)@BSA-AuNCs NPs increasing. The relative activity of cells was approximately 80% at the maximum concentration of IL@MIL-101(Fe)@BSA-AuNCs NPs. The result confirmed that IL@MIL-101(Fe)@BSA-AuNCs NPs possessed good biocompatibility [72], which could be further used *in vivo*.

To evaluate the biological toxicity of IL@MIL-101(Fe)@BSA-AuNCs NPs *in vivo*, the dose of 100 , 150 , $200\ \text{mg kg}^{-1}$ of IL@MIL-101(Fe)@BSA-AuNCs NPs was injected in mice by tail vein (PBS was used as the control). The result of body weight was shown in Fig. 6b. During the experimental period, the body weight of mice exhibited a slowly increasing trend. Compared with the control group, experimental groups showed no significantly different in body weight indexes. In order to further evaluate the toxicity of IL@MIL-101(Fe)@BSA-AuNCs NPs and their effect on the health of mice, blood routine test and blood biochemical test were performed as shown in Fig. S10. From the test results, the experimental groups were normal comparing with control group. The viscera index of liver and kidney in the group injected with $200\ \text{mg kg}^{-1}$ of IL@MIL-101(Fe)@BSA-AuNCs NPs was significantly higher than that of the control group, indicating that higher concentration of IL@MIL-101(Fe)@BSA-AuNCs NPs affected the health of mice. While there was no abnormality when the injected dose was $150\ \text{mg kg}^{-1}$, manifesting that the maximum tolerated dose of IL@MIL-101(Fe)@BSA-AuNCs NPs was approximately $150\ \text{mg kg}^{-1}$. As shown in Fig. S11, the H&E staining results of tissue sections (heart, liver, lung, spleen, and kidney) showed no obvious abnormalities in the experimental groups treated with different concentrations of the IL@MIL-101(Fe)@BSA-AuNCs NPs comparing with the control group. Above all, the IL@MIL-101(Fe)@BSA-AuNCs NPs possessed low toxicity and good biocompatibility characteristics.

3.6. Tumor diagnosis and degradation monitoring by dual-modality imaging *in vivo*

Tumor diagnosis is a prerequisite for cancer treatment. However, single-mode imaging of the tumor site cannot provide sufficient evidence for the exact tumor site and adequate features for different tumors. As traditional single-mode imaging technology, FI holds outstanding sensitivity at molecular level but has inherent drawbacks such as low penetration depth and poor spatial resolution. MRI overcomes the optical diffusion limitation, owns high spatial resolution but has shortcomings of low sensitivity. To solve these problems, many researchers have focused on developing multi-mode imaging probes and integrating various imaging enhancement behaviors into a single system to realize complementary imaging functions [37,73–76]. It is well-known that Fe^{3+} can quench the fluorescence of dyes and quantum dots [77]. In this work, a rapid assembly and coupling method was adopted to avoid the quench of BSA-Au NCs. The BSA-Au NCs were coupled on surface of IL@MIL-101(Fe) NPs to endow IL@MIL-101(Fe)@BSA-AuNCs NPs with dual-modality imaging function. Fig. 6a, e showed that IL@MIL-101(Fe)@BSA-AuNCs NPs possessed MRI and FI property *in vitro*. We measured plot of T2 relaxation rate ($1/T_2$) under different concentrations of IL@MIL-101(Fe)@BSA-AuNCs with $r^2 = 7.93086$ (Fig. 6a). The signal intensity of fluorescence and MR imaging of IL@MIL-101(Fe)@BSA-AuNCs NPs reached maximum at 5 h in the tumor after IL@MIL-101(Fe)@BSA-AuNCs NPs were injected by

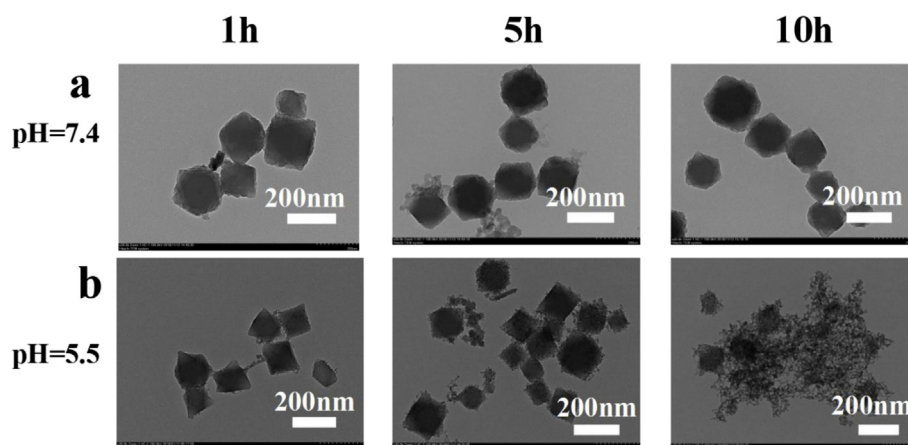


Fig. 4. (a) TEM images of MIL-101(Fe) NPs degrading in neutral phosphate buffer (pH = 7.4 PBS) at different time points (1 h, 5 h, 10 h). (b) TEM images of MIL-101(Fe) NPs degrading in acid phosphate buffer (pH = 5.5 PBS) at different time points (1 h, 5 h, 10 h).

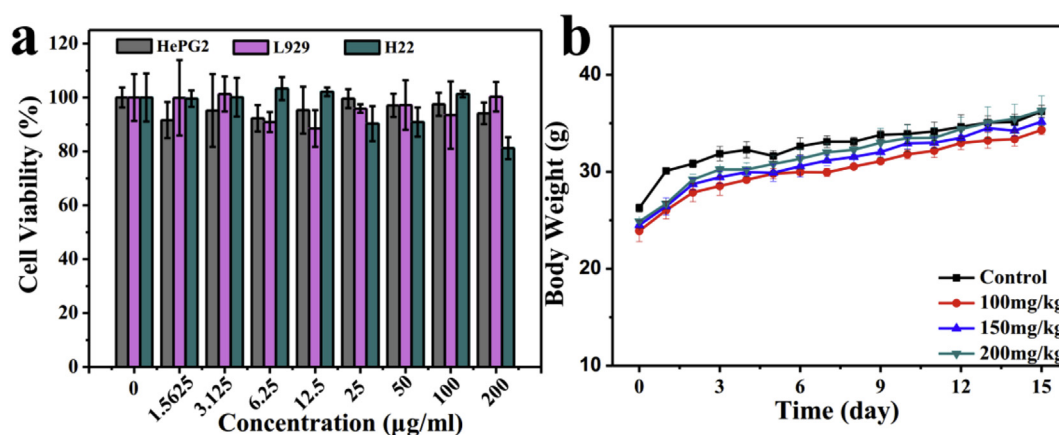


Fig. 5. Toxicity Experiment of IL@MIL-101(Fe)@BSA-AuNCs NPs *in vitro* and *in vivo*. (a) The viability of HepG2, L929, H22 cells was measured by MTT assay with different concentration of IL@MIL-101(Fe)@BSA-AuNCs NPs for 24 h. (b) Weight change of mice injected with different concentrations of IL@MIL-101(Fe)@BSA-AuNCs NPs for 14 days.

tail vein. The tumor site could be imaged, which was expected that IL@MIL-101(Fe)@BSA-AuNCs NPs could promote precise diagnosis of tumor after injecting for 5 h (Fig. 6e).

To explore the degradation and distribution process of MIL-101(Fe) NPs *in vivo*, the dual-mode imaging was also employed to study the degradation and distribution of MIL-101(Fe) NPs *in vivo*. The MRI signal intensity could directly determine degradation and distribution process of IL@MIL-101(Fe)@BSA-AuNCs NPs. When IL@MIL-101(Fe)@BSA-AuNCs NPs degraded slowly *in vivo*, Fe^{3+} was produced gradually, causing the fluorescence of IL@MIL-101(Fe)@BSA-AuNCs NPs to slowly disappear. With fluorescence of IL@MIL-101(Fe)@BSA-AuNCs NPs disappearing, the degradation of MIL-101(Fe) NPs was indirectly determined. As shown in Fig. 6b, MR images showed the dynamic distribution of IL@MIL-101(Fe)@BSA-AuNCs NPs in liver and tumor of tumor-bearing mice. Fig. 6c showed the T2-MR signal of liver and tumor, the T2-MR signal intensity reached maximum at 1 h in the liver and 5 h in the tumor during test for 10 h. Fig. 6f showed the biodistribution of IL@MIL-101(Fe)@BSA-AuNCs in liver, lung, spleen, kidney, heart, tumor, indicating that the fluorescence signal intensity is consistent with the intensity of MRI *in vivo*. Furthermore, the results confirmed that IL@MIL-101(Fe)@BSA-AuNCs NPs were degradable *in vivo*, which could be degraded *in vivo* by observing FI and MRI of IL@MIL-101(Fe)@BSA-AuNCs NPs. Moreover, the main organ for metabolism and distribution was liver, which was also confirmed by alanine aminotransferase (ALT), aspartate aminotransferase (AST) in blood biochemistry test. And tumor site could be imaged accurately. These

results indicated that as-obtained IL@MIL-101(Fe)@BSA-AuNCs NPs were biodegradable, and expected to be *in vivo* excreted out of the body after therapeutic functioning.

3.7. Evaluation of microwave enhancing dynamic effect and combination treatment of MTT and MEDT in tumor cells

In order to further verify the effect of MEDT in cells, cells were incubated with extracorporeal H_2O_2 . Due to cells at tumor site lose regulation and control of H_2O_2 , superfluous H_2O_2 would be generated. In this study, in order to simulate excess H_2O_2 generated at tumor site, we employed a method from the literature to explore a certain concentration that has no effect on cell growth by MTT assay [78–81]. As Fig. 7a shown that 60 μM was the criticality concentration, which was consistent with literature result that neither promoted cell growth nor inhibited cell growth. In the MEDT cell experiment, there were 9 groups being divided, HepG2 cells were incubated with H_2O_2 at 60 μM for 24 h in the groups containing H_2O_2 , then HepG2 cells were incubated with 100 $\mu\text{g mL}^{-1}$ of MIL-101(Fe) NPs for 24 h in the groups containing MIL-101(Fe). Then 1.0 mL of cells were treated under 0.9 W MW irradiation for 3 min at 5% glucose solution to avoid the heating effect. The cell viability of MIL-101(Fe) + H_2O_2 + MW group as experiment group was 47.7%, while H_2O_2 group, H_2O_2 + MW group, H_2O_2 + MIL-101(Fe) group were 102.8%, 90%, 85.6%, the data confirmed that MIL-101(Fe) NPs were cable of catalyzing H_2O_2 to generate $\cdot\text{OH}$ in a more efficient under MW irradiation, amount of $\cdot\text{OH}$ produced could destroy tumor

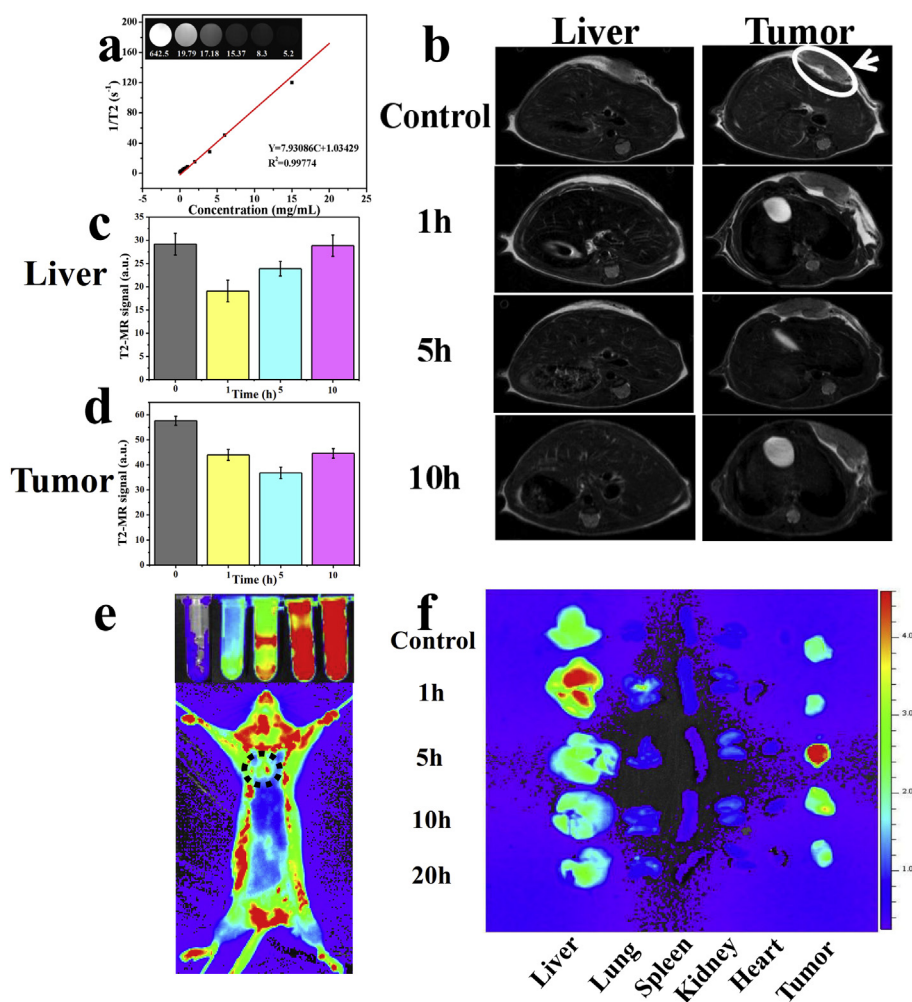


Fig. 6. Tumor diagnosis and degradation monitoring by dual-modality imaging *in vivo*. (a) T2-weighted MR images and T2 relaxation rate for various concentrations of IL@MIL-101(Fe)@BSA-AuNCs NPs. (b) Distribution process of IL@MIL-101(Fe)@BSA-AuNCs NPs *in vivo* at 1, 5, 10 h. (c) The T2-MR signal intensity of IL@MIL-101(Fe)@BSA-AuNCs NPs in liver at 1, 5, 10 h. (d) The T2-MR signal intensity of IL@MIL-101(Fe)@BSA-AuNCs NPs in tumor at 1, 5, 10 h. (e) The fluorescence imaging of IL@MIL-101(Fe)@BSA-AuNCs NPs *in vivo* and fluorescence imaging of different concentrations of IL@MIL-101(Fe)@BSA-AuNCs NPs *in vitro*. (f) *Ex vivo* fluorescence imaging of liver, lungs, spleen, kidneys, heart, tumor.

cells effectively (Fig. 7b). As shown in Fig. 7c, it was further evaluated anti-cancer effect by combination of MEDT and MTT in cells. The $100 \mu\text{g mL}^{-1}$ of IL@MIL-101(Fe)@BSA-AuNCs NPs were incubated into cells overnight, the MW group and IL@MIL-101(Fe)@BSA-AuNCs + MW group were treated with MW irradiation at 0.9 W for 0, 3, 5, 8 min, then the relative viability of cells was calculated by MTT assay respectively. It could be clearly seen from Fig. 7c that as the microwave time increased, the cell viability of the IL@MIL-101(Fe)@BSA-AuNCs + MW group became less and less, and the relative viability of the cells decreased from 86.5% to 33.6%. When the microwave time is the same, the cell viability of the IL@MIL-101(Fe)@BSA-

AuNCs + MW group was significantly lower than the MW group and IL@MIL-101(Fe)@BSA-AuNCs group, which demonstrated that IL@MIL-101(Fe)@BSA-AuNCs NPs could destroy effectively the cancer cells by combination of MEDT and MTT.

3.8. Tumor therapy experiment

The IL@MIL-101(Fe)@BSA-AuNCs NPs could promote the increase in temperature and the generation of $\cdot\text{OH}$ under MW irradiation *in vitro*, thus the anti-tumor effect of IL@MIL-101(Fe)@BSA-AuNCs NPs by combining MTT with MEDT need be further verified *in vivo*. The tumor

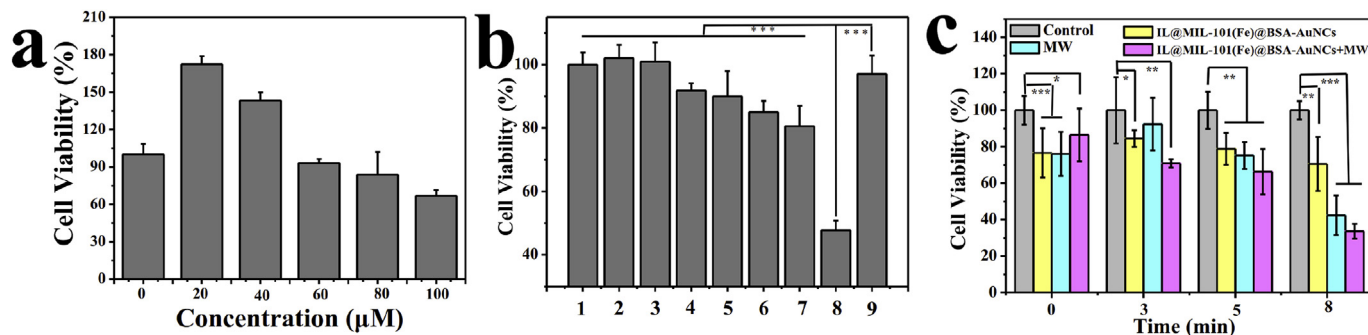
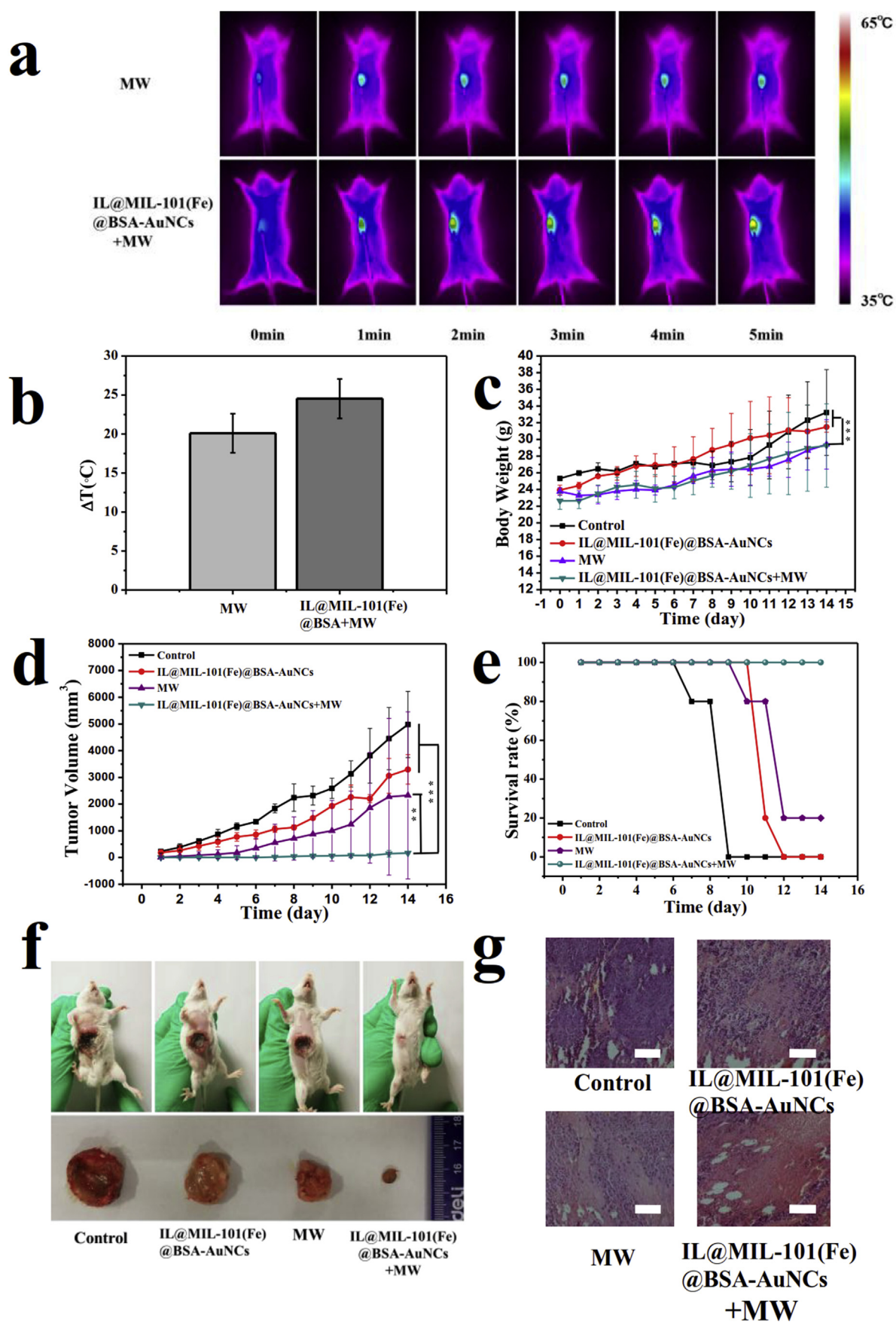


Fig. 7. Evaluation of microwave dynamic enhancing effect and combination treatment of MTT and MEDT in tumor cells. (a) The viability of HepG2 cells measured by MTT assay incubating cells with different concentration of H_2O_2 for 24 h. (b) MEDT validation on cells. (1-9: Control, H_2O_2 , MIL-101(Fe), MW, H_2O_2 + MW, MIL-101(Fe) + MW, H_2O_2 + MIL-101(Fe) + MW, $\text{C}_6\text{H}_{12}\text{O}_6$ groups). (c) The viability of HepG2 cells by incubated with $100 \mu\text{g mL}^{-1}$ IL@MIL-101(Fe)@BSA-AuNCs NPs for 24 h under MW irradiation at 0.9 W for 3, 5 and 8 min (* indicates $p < 0.05$, ** indicates $p < 0.01$, *** indicates $p < 0.001$).



(caption on next page)

Fig. 8. Tumor therapy experiment *in vivo*. (a) Tumor treatment images of mice injected with IL@MIL-101(Fe)@BSA-AuNCs NPs via intravenous. (b) Temperature curve at the tumor site by comparing with MW group and IL@MIL-101(Fe)@BSA-AuNCs + MW group. (c) Weight changes of mice bearing H22 tumor treated by microwave needle for 14 days. (d) Changes of tumor volume of mice bearing H22 tumor treated by microwave needle for 14 days. (e) Survival rates of mice being treated for 14 days. (f) Tumor photos and tumor-bearing mice photos after 14 days. (g) Comparing different groups of tumor tissue sections. (The scale bar is 50 μ m, ** indicates $p < 0.01$, *** indicates $p < 0.001$).

therapy effect of IL@MIL-101(Fe)@BSA-AuNCs NPs was further validated in mice. 20 experimental mice were divided into control, IL@MIL-101(Fe)@BSA-AuNCs, MW, IL@MIL-101(Fe)@BSA-AuNCs + MW group. In addition, the optimal tumor treatment time was 5 h after intravenous injection according to the strongest signal intensity of MRI, FI and the maximum content of Au at tumor site by ICP analysis (Fig. S12). In Fig. 8a, the FLIR imaging instrument was used to record the change process of corresponding temperature of the MW group and the IL@MIL-101(Fe)@BSA-AuNCs + MW group. The IL@MIL-101(Fe)@BSA-AuNCs + MW group was significantly higher than that of the MW group in tumor region. The maximum temperature difference between the MW group and the IL@MIL-101(Fe)@BSA-AuNCs + MW group was 5 °C (Fig. 8b). It indicated that IL@MIL-101(Fe)@BSA-AuNCs NPs with excellent heating sensitivity also had better effect *in vivo*. In Fig. 8c, it showed the change in body weight of tumor-bearing H22 mice after MTT and MEDT, each group of mice weight slowly rose. The tumor volume in the IL@MIL-101(Fe)@BSA-AuNCs + MW group was the smallest by comparing with mice in different experimental groups. It has shown that the control group had the largest tumor volume. The IL@MIL-101(Fe)@BSA-AuNCs group only exhibited chemical therapy effect comparing with the control group, the MW group only exhibited hyperthermia effect, IL@MIL-101(Fe)@BSA-AuNCs + MW group exhibited the treatment effect of by combining MTT and MEDT (Fig. 8d). As shown in Fig. 8e, the survival rate of MW group was 20%, the survival rate of control group and IL@MIL-101(Fe)@BSA-AuNCs group was 0%. While the survival rate of IL@MIL-101(Fe)@BSA-AuNCs + MW group reached 100%, indicating that had the excellent tumor-inhibitory effect (We determined that the mice have been dead when the tumor volume exceeded 2000 mm³ due to animal welfare). The synergy of MTT and MEDT proved that IL@MIL-101(Fe)@BSA-AuNCs + MW had excellently therapeutic effect on tumor-bearing mice. Images of tumors in different groups after treatment for 14 days were consistent with the line chart of tumor volume (Fig. 8f). The tissues of the mice were finally collected, including spleen, liver, kidney, lung and tumor. The obtained tissues were stained with hematoxylin and eosin (H&E). Histologic section was no significant difference by comparing with the other groups as shown in Fig. S13. Compared with the other groups, the tumor necrosis area of IL@MIL-101(Fe)@BSA-AuNCs + MW group was the largest, which exhibited distinct anti-cancer effect (Fig. 8g).

4. Conclusion

In conclusion, we fabricated biodegradable IL@MIL-101(Fe)@BSA-AuNCs NPs possessing peroxidase-like catalytic activity and dual-modality imaging property. MIL-101(Fe) NPs as nanozymes, enabled to catalyze H₂O₂ to generate ·OH and accelerate to generate abundant ·OH under MW irradiation in tumor microenvironment due to good MW conversion capability and intrinsic enzyme-mimicking property. As-made IL@MIL-101(Fe)@BSA-AuNCs NPs with MRI and FI function not only monitored dynamic distribution process in the body but also diagnosed accurate tumor site. Accurate diagnosis and synergistic treatment of MEDT and MTT are concentrated on IL@MIL-101(Fe)@BSA-AuNCs NPs, which shows great potential for improving tumor treatment effect.

Acknowledgements

The authors acknowledge financial support from the National Key R

&D Program (2018YFC0115503, 2018YFC0115500), National Natural Science Foundation of China (Nos. 81630053, 61671435, 61571426), CAS-DOE program (No. GJHZ1705), and Beijing Natural Science Foundation (No. 4161003).

Appendix A. Supplementary data

Supplementary data to this article can be found online at <https://doi.org/10.1016/j.biomaterials.2019.119223>.

References

- [1] X. Lian, Y. Fang, E. Joseph, Q. Wang, J. Li, S. Banerjee, C. Lollar, X. Wang, H.C. Zhou, Enzyme-MOF (metal-organic framework) composites, *Chem. Soc. Rev.* 46 (11) (2017) 3386–3401.
- [2] M. Huo, L. Wang, Y. Chen, J. Shi, Tumor-selective catalytic nanomedicine by nanocatalyst delivery, *Nat. Commun.* 8 (1) (2017) 357–369.
- [3] Z. Wang, Y. Zhang, E. Ju, Z. Liu, F. Cao, Z. Chen, J. Ren, X. Qu, Biomimetic nanoflowers by self-assembly of nanozymes to induce intracellular oxidative damage against hypoxic tumors, *Nat. Commun.* 9 (1) (2018) 3334–3348.
- [4] Y. Huang, J. Ren, X. Qu, Nanozymes: Classification, catalytic mechanisms, activity regulation, and applications, *Chem. Rev.* 119 (6) (2019) 4357–4412.
- [5] J. Wu, X. Wang, Q. Wang, Z. Lou, S. Li, Y. Zhu, L. Qin, H. Wei, Nanomaterials with enzyme-like characteristics (nanozymes): Next-generation artificial enzymes (II), *Chem. Soc. Rev.* 48 (4) (2019) 1004–1076.
- [6] S. Park, A. Aalipour, O. Vermesh, J.H. Yu, S.S. Gambhir, Towards clinically translatable *in vivo* nanodiagnostics, *Nat. Rev. Mater.* 2 (2017) 17014.
- [7] X. Li, J. Kim, J. Yoon, X. Chen, Stimuli-Driven Cancer-Associated, Turn on theranostics for multimodality imaging and therapy, *Adv. Mater.* 29 (23) (2017) 1606857–1606881 29 (23).
- [8] L. Gao, J. Zhuang, L. Nie, J. Zhang, Y. Zhang, N. Gu, T. Wang, J. Feng, D. Yang, S. Perrett, Intrinsic peroxidase-like activity of ferromagnetic nanoparticles, *Nat. Nanotechnol.* 2 (9) (2007) 577–583.
- [9] P. Prasad, C.R. Gordijo, A.Z. Abbasi, A. Maeda, A. Ip, A.M. Rauth, R.S. Dacosta, X.Y. Wu, Multifunctional albumin-MnO₂ nanoparticles modulate solid tumor microenvironment by attenuating hypoxia, acidosis, vascular endothelial growth factor and enhance radiation response, *ACS Nano* 8 (6) (2014) 3202–3212.
- [10] M. Li, Z. Qi, Y. Xuan, X. Zhong, G. Song, Z. Chai, L. Zhuang, Y. Kai, Au@MnS@ZnS core/shell/shell nanoparticles for magnetic resonance imaging and enhanced cancer radiation therapy, *ACS Appl. Mater. Interfaces* 8 (15) (2016) 9557–9564.
- [11] Y. Zhang, F. Wang, C. Liu, Z. Wang, L. Kang, Y. Huang, K. Dong, J. Ren, X. Qu, Nanozyme decorated metal-organic frameworks for enhanced photodynamic therapy, *ACS Nano* 12 (1) (2018) 651–661.
- [12] J.Y. Zeng, M.Z. Zou, M. Zhang, X.S. Wang, X. Zeng, H. Cong, X.Z. Zhang, Pi-extended benzoporphyrin-based metal-organic framework for inhibition of tumor metastasis, *ACS Nano* 12 (5) (2018) 4630–4640.
- [13] C. Zhang, W. Bu, D. Ni, S. Zhang, Q. Li, Z. Yao, J. Zhang, H. Yao, Z. Wang, J. Shi, Synthesis of iron nanometallic glasses and their application in cancer therapy by a localized Fenton reaction, *Angew. Chem. Int. Ed. Engl.* 55 (6) (2016) 2101–2106.
- [14] C. Fu, H. Zhou, L. Tan, Z. Huang, Q. Wu, X. Ren, J. Ren, X. Meng, Microwave-activated Mn-doped zirconium metal-organic framework nanocubes for highly effective combination of microwave dynamic and thermal therapies against cancer, *ACS Nano* 12 (3) (2018) 2201–2210.
- [15] D. Long, T. Liu, L. Tan, H. Shi, P. Liang, S. Tang, Q. Wu, J. Yu, J. Dou, X. Meng, Multisynthetic platform for tumor therapy by mild microwave irradiation-activated chemotherapy and enhanced ablation, *ACS Nano* 10 (10) (2016) 9516–9528.
- [16] R. Freund, U. Lachelt, T. Gruber, B. Rühle, S. Wuttke, Multifunctional efficiency: Extending the concept of atom economy to functional nanomaterials, *ACS Nano* 12 (3) (2018) 2094–2105.
- [17] O.Y. Lyakin, R.V. Ottenbacher, K.P. Bryliakov, E.P. Talsi, Asymmetric epoxidations with H₂O₂ on Fe and Mn aminopyridine catalysts: Probing the nature of active species by combined electron paramagnetic resonance and enantioselectivity study, *ACS Catal.* 2 (6) (2012) 1196–1202.
- [18] Y. Yang, W. Zhu, L. Feng, Y. Chao, X. Yi, Z. Dong, K. Yang, W. Tan, Z. Liu, M. Chen, G-Quadruplex-Based nanoscale coordination polymers to modulate tumor hypoxia and achieve nuclear-targeted drug delivery for enhanced photodynamic therapy, *Nano Lett.* 18 (11) (2018) 6867–6875.
- [19] Y. Yang, W. Zhu, Z. Dong, Y. Chao, L. Xu, M. Chen, Z. Liu, 1D coordination polymer nanofibers for low-temperature photothermal therapy, *Adv. Mater.* 29 (40) (2017) 201703588.
- [20] J. Crossgrove, W. Zheng, Manganese toxicity upon overexposure, *NMR Biomed.* 17 (8) (2004) 544–553.
- [21] Y. Yang, F. Xia, Y. Yang, B. Gong, A. Xie, Y. Shen, M. Zhu, Litchi-like Fe₃O₄@Fe-MOF capped with HAp gatekeepers for pH-triggered drug release and anticancer

- effect, *J. Mater. Chem. B* 5 (43) (2017) 8600–8606.
- [22] M. Huo, C. Yu, J. Shi, Triggered-release drug delivery nanosystems for cancer therapy by intravenous injection: Where are we now? *Expert Opin. Drug Deliv.* 13 (9) (2016) 1–4.
- [23] B.P. Purcell, L. David, M.B. Charati, S.M. Dorsey, R.J. Wade, K.N. Zellars, D. Heather, P. Sara, C.B. Logdon, J.A. Shuman, Injectable and bioresponsive hydrogels for on-demand matrix metalloproteinase inhibition, *Nat. Mater.* 13 (6) (2014) 653–661.
- [24] M.W. Tibbitt, J.E. Dahlman, R. Langer, ChemInform abstract: Emerging frontiers in drug delivery, *ChemInform* 47 (19) (2016) 704–717.
- [25] M.E. Calderera-Moore, W.B. Liechty, N.A. Peppas, Responsive theranostic systems: Integration of diagnostic imaging agents and responsive controlled release drug delivery carriers, *Accounts Chem. Res.* 44 (10) (2011) 1061–1070.
- [26] C. Huachao, H. Weijiang, G. Zijian, An H₂O₂-responsive nanocarrier for dual-release of platinum anticancer drugs and O₂: Controlled release and enhanced cytotoxicity against cisplatin resistant cancer cells, *Chem. Commun.* 50 (68) (2014) 9714–9717.
- [27] B.W. Yang, Y. Chen, J.L. Shi, Nanozymes in catalytic cancer theranostics, *Prog. Biochem. Biophys.* 45 (2) (2018) 237–255.
- [28] Q. Chen, M. Xu, W. Zheng, T. Xu, H. Deng, J. Liu, Se/Ru-Decorated porous metal-organic framework nanoparticles for the delivery of pooled siRNAs to reversing multidrug resistance in taxol-resistant breast cancer cells, *ACS Appl. Mater. Interfaces* 9 (8) (2017) 6712–6724.
- [29] X. Chen, M. Zhang, S. Li, L. Li, L. Zhang, T. Wang, M. Yu, Z. Mou, C. Wang, Facile synthesis of polypyrrole@metal-organic framework core-shell nanocomposites for dual-mode imaging and synergistic chemo-photothermal therapy of cancer cells, *J. Mater. Chem. B* 5 (9) (2017) 1772–1778.
- [30] F. Hu, D. Mao, Kenry, Y. Wang, W. Wu, D. Zhao, D. Kong, B. Liu, Metal-organic framework as a simple and general inert nanocarrier for photosensitizers to implement activatable photodynamic therapy, *Adv. Funct. Mater.* 28 (19) (2018) 1707519.
- [31] B. Illes, P. Hirschle, S. Barnert, V. Cauda, S. Wuttke, H. Engelke, Exosome-Coated metal-organic framework nanoparticles: An efficient drug delivery platform, *Chem. Mater.* 29 (19) (2017) 8042–8046.
- [32] X. Jiang, Z. Wang, H. Wang, Y. Zhuo, R. Yuan, Y. Chai, A novel metal-organic framework loaded with abundant N-(aminobutyl)-N-(ethylisoluminol) as a high-efficiency electrochemiluminescence indicator for sensitive detection of mucin1 on cancer cells, *Chem. Commun.* 53 (70) (2017) 9705–9708.
- [33] G. Lan, K. Ni, Z. Xu, S.S. Veroneau, Y. Song, W. Lin, Nanoscale metal-organic framework overcomes hypoxia for photodynamic therapy primed cancer immunotherapy, *J. Am. Chem. Soc.* 140 (17) (2018) 5670–5673.
- [34] M. Lismont, L. Dreesen, S. Wuttke, Metal-organic framework nanoparticles in photodynamic therapy: Current status and perspectives, *Adv. Funct. Mater.* 27 (14) (2017) 1606314.
- [35] Y. Luo, S. Fan, W. Yu, Z. Wu, D.A. Cullen, C. Liang, J. Shi, C. Su, Fabrication of Au25(SG)18-ZIF-8 nanocomposites: A facile strategy to position Au25 (SG)18 nanoclusters inside and outside ZIF-8, *Adv. Mater.* 30 (6) (2018) 1704576–1704585.
- [36] D. Mao, F. Hu, Kenry, S. Ji, W. Wu, D. Ding, D. Kong, B. Liu, Metal-organic-framework-assisted in vivo bacterial metabolic labeling and precise antibacterial therapy, *Adv. Mater.* 30 (18) (2018) 1706831–170687.
- [37] W. Shang, C. Zeng, Y. Du, H. Hui, X. Liang, C. Chi, K. Wang, Z. Wang, J. Tian, Core-Shell gold Nanorod@Metal-organic framework nanoprobe for multimodality diagnosis of glioma, *Adv. Mater.* 29 (3) (2017) 1604381–1604388.
- [38] D. Wang, J. Zhou, R. Chen, R. Shi, C. Wang, J. Lu, G. Zhao, G. Xia, S. Zhou, Z. Liu, H. Wang, Z. Guo, Q. Chen, Core-Shell metal-organic frameworks as Fe²⁺ suppliers for Fe²⁺-mediated cancer therapy under multimodality imaging, *Chem. Mater.* 29 (8) (2017) 3477–3489.
- [39] Y. Yang, J. Liu, C. Liang, L. Feng, T. Fu, Z. Dong, Y. Chao, Y. Li, G. Lu, M. Chen, Z. Liu, Nanoscale metal-organic frameworks with rapid clearance for magnetic resonance imaging-guided photothermal therapy, *ACS Nano* 10 (2) (2016) 2774–2781.
- [40] J. Liu, Y. Yang, W. Zhu, X. Yi, Z. Dong, X. Xu, M. Chen, K. Yang, G. Lu, L. Jiang, Z. Liu, Nanoscale metal-organic frameworks for combined photodynamic & radiation therapy in cancer treatment, *Biomaterials* 97 (2016) 1–9.
- [41] M.H. Teplensky, M. Pantham, P. Li, T.C. Wang, J.P. Mehta, L.J. Young, P.Z. Moghadam, J.T. Hupp, O.K. Farha, C.F. Kaminski, D. Fairen-Jimenez, Temperature treatment of highly porous zirconium-containing metal-organic frameworks extends drug delivery release, *J. Am. Chem. Soc.* 139 (22) (2017) 7522–7532.
- [42] S. Wuttke, S. Braig, T. Preiss, A. Zimpel, J. Sicklinger, C. Bellomo, J.O. Radler, A.M. Vollmar, T. Bein, MOF nanoparticles coated by lipid bilayers and their uptake by cancer cells, *Chem. Commun.* 51 (87) (2015) 15752–15755.
- [43] C. He, K. Lu, W. Lin, Nanoscale metal-organic frameworks for real-time intracellular pH sensing in live cells, *J. Am. Chem. Soc.* 136 (35) (2014) 12253–12256.
- [44] S. Wuttke, M. Lismont, A. Escudero, B. Rungtaweewanit, W.J. Parak, Positioning metal-organic framework nanoparticles within the context of drug delivery - a comparison with mesoporous silica nanoparticles and dendrimers, *Biomaterials* 123 (2017) 172–183.
- [45] H. Patricia, C. Tamim, S. Christian, G. Brigitte, S. Catherine, B. Tarek, J.F. Eubank, H. Daniela, C. Pascal, K. Christine, Porous metal-organic-framework nanoscale carriers as a potential platform for drug delivery and imaging, *Nat. Mater.* 9 (2) (2010) 172–178.
- [46] F. Masselot, A. Boulos, M. Maurin, J.M. Rolain, D. Raoult, PYRAMIR: Calibration and operation of a pyramid near-infrared wavefront sensor, *Publ. Astron. Soc. Pac.* 120 (870) (2008) 872–886.
- [47] S. Rojas, T. Baati, L. Njim, L. Manchego, F. Neffati, N. Abdeljelil, S. Saguem, C. Serre, M.F. Najjar, A. Zakhama, P. Horcajada, Metal-organic frameworks as efficient oral detoxifying agents, *J. Am. Chem. Soc.* 140 (30) (2018) 9581–9586.
- [48] T. Simon-Yarza, A. Mielcarek, P. Couvreur, C. Serre, Nanoparticles of metal-organic frameworks: On the road to in vivo efficacy in biomedicine, *Adv. Mater.* 30 (37) (2018) 1707365–1707380.
- [49] B. Illes, S. Wuttke, H. Engelke, Liposome-Coated iron fumarate metal-organic framework nanoparticles for combination therapy, *Nanomaterials* 7 (11) (2017) 351–362.
- [50] K. Lu, C. He, N. Guo, C. Chan, K. Ni, G. Lan, H. Tang, C. Pelizzari, Y.-X. Fu, M.T. Spiotto, R.R. Weichselbaum, W. Lin, Low-dose X-ray radiotherapy-radiodynamic therapy via nanoscale metal-organic frameworks enhances checkpoint blockade immunotherapy, *Nat. Biomed. Eng.* 2 (8) (2018) 600–610.
- [51] J.Y. Zeng, M.Z. Zou, M. Zhang, X.S. Wang, X. Zeng, H. Cong, X.Z. Zhang, I. Extended benzoporphyrin-based metal-organic framework for inhibition of tumor metastasis, *ACS Nano* 12 (5) (2018) 4630–4640.
- [52] S.Y. Li, H. Cheng, B.R. Xie, W.X. Qiu, J.Y. Zeng, C.X. Li, S.S. Wan, L. Zhang, W.L. Liu, X.Z. Zhang, Cancer cell membrane camouflaged cascade bioreactor for cancer targeted starvation and photodynamic therapy, *ACS Nano* 11 (7) (2017) 7006–7018.
- [53] M. Xu, S. Yuan, X.Y. Chen, Y.J. Chang, G. Day, Z.Y. Gu, H.C. Zhou, Two-dimensional metal-organic framework nanosheets as an enzyme inhibitor: Modulation of the alpha-chymotrypsin activity, *J. Am. Chem. Soc.* 139 (24) (2017) 8312–8319.
- [54] F.K. Shieh, S.C. Wang, C.I. Yen, C.C. Wu, S. Dutta, L.Y. Chou, J.V. Morabito, P. Hu, M.H. Hsu, K.C. Wu, C.K. Tsung, Imparting functionality to biocatalysts via embedding enzymes into nanoporous materials by a de novo approach: Size-selective sheltering of catalase in metal-organic framework microcrystals, *J. Am. Chem. Soc.* 137 (13) (2015) 4276–4279.
- [55] T. Simon-Yarza, M. Gimenez-Marques, R. Mrimi, A. Mielcarek, R. Gref, P. Horcajada, C. Serre, P. Couvreur, A smart metal-organic framework nanomaterial for lung targeting, *Angew. Chem. Int. Ed. Engl.* 56 (49) (2017) 15565–15569.
- [56] Y. Hu, H. Cheng, X. Zhao, J. Wu, F. Muhammad, S. Lin, J. He, L. Zhou, C. Zhang, Y. Deng, P. Wang, Z. Zhou, S. Nie, H. Wei, Surface-enhanced Raman scattering active gold nanoparticles with enzyme-mimicking activities for measuring glucose and lactate in living tissues, *ACS Nano* 11 (6) (2017) 5558–5566.
- [57] H. Shi, M. Niu, L. Tan, T. Liu, H. Shao, C. Fu, X. Ren, T. Ma, J. Ren, L. Li, H. Liu, K. Xu, J. Wang, F. Tang, X. Meng, A smart all-in-one theranostic platform for CT imaging guided tumor microwave thermotherapy based on IL@ZrO₂ nanoparticles, *Chem. Sci.* 6 (8) (2015) 5016–5026.
- [58] L. Qin, G. Zeng, C. Lai, D. Huang, P. Xu, C. Zhang, M. Cheng, X. Liu, S. Liu, B. Li, H. Yi, “Gold rush” in modern science: Fabrication strategies and typical advanced applications of gold nanoparticles in sensing, *Coord. Chem. Rev.* 359 (2018) 1–31.
- [59] L. Qin, G. Zeng, C. Lai, D. Huang, C. Zhang, P. Xu, T. Hu, X. Liu, M. Cheng, Y. Liu, L. Hu, Y. Zhou, A visual application of gold nanoparticles: Simple, reliable and sensitive detection of kanamycin based on hydrogen-bonding recognition, *Sensor. Actuator. B Chem.* 243 (2017) 946–954.
- [60] L. Qin, D. Huang, P. Xu, G. Zeng, C. Lai, Y. Fu, H. Yi, B. Li, C. Zhang, M. Cheng, C. Zhou, X. Wen, In-situ deposition of gold nanoparticles onto polydopamine-decorated g-C₃N₄ for highly efficient reduction of nitroaromatics in environmental water purification, *J. Colloid Interface Sci.* 534 (2019) 357–369.
- [61] L. Qin, G. Zeng, C. Lai, D. Huang, C. Zhang, M. Cheng, H. Yi, X. Liu, C. Zhou, W. Xiong, F. Huang, W. Cao, Synthetic strategies and application of gold-based nanocatalysts for nitroaromatics reduction, *Sci. Total Environ.* 652 (2019) 93–116.
- [62] J. Xie, Y. Zheng, J.Y. Ying, Protein-directed synthesis of highly fluorescent gold nanoclusters, *J. Am. Chem. Soc.* 131 (3) (2009) 888.
- [63] Z. Dong, Y. Sun, J. Chu, X. Zhang, H. Deng, Multivariate metal-organic frameworks for dialing in the binding and programming the release of drug molecules, *J. Am. Chem. Soc.* 139 (40) (2017) 14209–14216.
- [64] G. Férey, C. Mellot-Draznieks, C. Serre, F. Millange, J. Dutour, S. Surblé, I. Margiolaki, A chromium terephthalate-based solid with unusually large pore volumes and surface area, *Science* 309 (5743) (2005) 2040–2042.
- [65] M. Yao, L. Ma, L. Li, J. Zhang, R.X. Lim, W. Chen, Y. Zhang, A new modality for cancer treatment—nanoparticle mediated microwave induced photodynamic therapy, *J. Biomed. Nanotechnol.* 12 (10) (2016) 1835–1851.
- [66] X. Chu, K. Li, H. Guo, H. Zheng, S. Shuda, X. Wang, J. Zhang, W. Chen, Y. Zhang, Exploration of graphitic-C₃N₄ quantum dots for microwave-induced photodynamic therapy, *ACS Biomater. Sci. Eng.* 3 (8) (2017) 1836–1844.
- [67] S. Gao, H. Lin, H. Zhang, H. Yao, Y. Chen, J. Shi, Nanocatalytic tumor therapy by biomimetic dual inorganic nanozyme-catalyzed cascade reaction, *Adv. Sci.* 5 (11) (2018) 1–12.
- [68] Q. Xiao, Z. Si, J. Zhang, C. Xiao, X. Tan, Photoinduced hydroxyl radical and photocatalytic activity of samarium-doped TiO₂ nanocrystalline, *J. Hazard Mater.* 150 (1) (2008) 62–67.
- [69] Q. Wu, M. Niu, X. Chen, L. Tan, C. Fu, X. Ren, J. Ren, L. Li, K. Xu, H. Zhong, X. Meng, Biocompatible and biodegradable zeolitic imidazolate framework/polydopamine nanocarriers for dual stimulus triggered tumor thermo-chemotherapy, *Biomaterials* 162 (2018) 132–143.
- [70] X. Unamuno, E. Imbuluzqueta, F. Salles, P. Horcajada, M.J. Blanco-Prieto, Biocompatible porous metal-organic framework nanoparticles based on Fe or Zr for gentamicin vectorization, *Eur. J. Pharm. Biopharm.* 132 (2018) 11–18.
- [71] C. Xu, Y. Wang, C. Zhang, Y. Jia, Y. Luo, X. Gao, AuGd integrated nanoprobe for optical/MRI/CT triple-modal in vivo tumor imaging, *Nanoscale* 9 (13) (2017) 4620–4628.
- [72] W. Hou, F. Xia, G. Alfranca, H. Yan, X. Zhi, Y. Liu, C. Peng, C. Zhang, J.M. de la Fuente, D. Cui, Nanoparticles for multi-modality cancer diagnosis: Simple protocol for self-assembly of gold nanoclusters mediated by gadolinium ions, *Biomaterials* 120 (2017) 103–114.

- [75] S. Yun, Z. Xingjun, P. Juanjuan, L. Fuyou, Core-shell lanthanide upconversion nanophosphors as four-modal probes for tumor angiogenesis imaging, *ACS Nano* 7 (12) (2013) 11290–11300.
- [76] J.Y. Zhu, M.K. Zhang, X.G. Ding, W.X. Qiu, W.Y. Yu, J. Feng, X.Z. Zhang, Virus-inspired nanogenes free from man-made materials for host-specific transfection and bio-aided MR imaging, *Adv. Mater.* 33 (22) (2018) 1707459–1707467.
- [77] H. Li, H. Huang, J.J. Feng, X. Luo, K.M. Fang, Z.G. Wang, A.J. Wang, A polypeptide-mediated synthesis of green fluorescent gold nanoclusters for Fe(3+) sensing and bioimaging, *J. Colloid Interface Sci.* 506 (2017) 386–392.
- [78] P.J. Chua, B.H. Yip, G.W. Yip, Cell cycle arrest induced by hydrogen peroxide is associated with modulation of oxidative stress related genes in breast cancer cells, *Exp. Biol. Med.* 234 (9) (2009) 1086–1094.
- [79] K. Barnouin, M.L. Dubuisson, E.S. Child, S. Fernandez de Mattos, J. Glassford, R.H. Medema, D.J. Mann, E.W. Lam, H₂O₂ induces a transient multi-phase cell cycle arrest in mouse fibroblasts through modulating cyclin D and p21Cip1 expression, *J. Biol. Chem.* 277 (16) (2002) 13761–13770.
- [80] D. Upadhyay, W. Chang, K. Wei, M. Gao, G.D. Rosen, Fibroblast growth factor-10 prevents H₂O₂-induced cell cycle arrest by regulation of G1 cyclins and cyclin dependent kinases, *FEBS Lett.* 581 (2) (2007) 248–252.
- [81] P.J. Chua, G.W. Yip, B.H. Bay, Cell cycle arrest induced by hydrogen peroxide is associated with modulation of oxidative stress related genes in breast cancer cells, *Exp. Biol. Med.* 234 (9) (2009) 1086–1094.